Polarization sensitive optical frequency domain imaging system for endobronchial imaging

Li, J.; Feroldi, Fabio; de Lange, J.; Daniels, J.M.A.; Grünberg, K.; de Boer, J.F.

published in
Optics Express
2015

DOI (link to publisher)
10.1364/OE.23.003390

document version
Publisher's PDF, also known as Version of record

Polarization sensitive optical frequency domain imaging system for endobronchial imaging

Jianan Li,[1] Fabio Feroldi,[1] Joop de Lange,[2] Johannes M. A. Daniels,[2] Katrien Grünberg[3] and Johannes F. de Boer[1,*]

[1]*Institute for Lasers, Life and Biophotonics Amsterdam, Department of Physics and Astronomy, VU University Amsterdam, De Boelelaan 1081, 1081 HV Amsterdam, The Netherlands*
[2]*VU University Medical Center, Department of Pulmonary Diseases, De Boelelaan 1117, Amsterdam, The Netherlands*
[3]*VU University Medical Center, Department of Pathology, De Boelelaan 1117, Amsterdam, The Netherlands*
**jfdeboer@few.vu.nl*

Abstract: A polarization sensitive endoscopic optical frequency domain imaging (PS-OFDI) system with a motorized distal scanning catheter is demonstrated. It employs a passive polarization delay unit to multiplex two orthogonal probing polarization states in depth, and a polarization diverse detection unit to detect interference signal in two orthogonal polarization channels. Per depth location four electro-magnetic field components are measured that can be represented in a complex 2x2 field matrix. A Jones matrix of the sample is derived and the sample birefringence is extracted by eigenvalue decomposition. The condition of balanced detection and the polarization mode dispersion are quantified. A complex field averaging method based on the alignment of randomly pointing field phasors is developed to reduce speckle noise. The variation of the polarization states incident on the tissue due to the circular scanning and catheter sheath birefringence is investigated. With this system we demonstrated imaging of ex vivo chicken muscle, in vivo pig lung and ex vivo human lung specimens.

OCIS codes: (170.2150) Endoscopic imaging; (170.4500) Optical coherence tomography; (260.5430) Polarization; (260.1440) Birefringence.

References and links

1. D. Huang, E. A. Swanson, C. P. Lin, J. S. Schuman, W. G. Stinson, W. Chang, M. R. Hee, T. Flotte, K. Gregory, C. A. Puliafito, and J. Fujimoto, "Optical coherence tomography," Science **254**(5035), 1178–1181 (1991).
2. W. Drexler and J. G. Fujimoto, "State-of-the-art retinal optical coherence tomography," Prog. Retin. Eye Res. **27**(1), 45–88 (2008).
3. G. J. Tearney, M. E. Brezinski, B. E. Bouma, S. A. Boppart, C. Pitris, J. F. Southern, and J. G. Fujimoto, "In vivo endoscopic optical biopsy with optical coherence tomography," Science **276**(5321), 2037–2039 (1997).
4. M. V. Sivak, Jr., K. Kobayashi, J. A. Izatt, A. M. Rollins, R. Ung-Runyawee, A. Chak, R. C. K. Wong, G. A. Isenberg, and J. Willis, "High-resolution endoscopic imaging of the GI tract using optical coherence tomography," Gastrointest. Endosc. **51**(4 Pt 1), 474–479 (2000).
5. S. Lam, B. Standish, C. Baldwin, A. McWilliams, J. leRiche, A. Gazdar, A. I. Vitkin, V. Yang, N. Ikeda, and C. MacAulay, "In vivo optical coherence tomography imaging of preinvasive bronchial lesions," Clin. Cancer Res. **14**(7), 2006–2011 (2008).
6. V. X. D. Yang, M. Gordon, S. J. Tang, N. Marcon, G. Gardiner, B. Qi, S. Bisland, E. Seng-Yue, S. Lo, J. Pekar, B. Wilson, and I. Vitkin, "High speed, wide velocity dynamic range Doppler optical coherence tomography (Part III): in vivo endoscopic imaging of blood flow in the rat and human gastrointestinal tracts," Opt. Express **11**(19), 2416–2424 (2003).
7. J. Li, M. de Groot, F. Helderman, J. Mo, J. M. A. Daniels, K. Grünberg, T. G. Sutedja, and J. F. de Boer, "High speed miniature motorized endoscopic probe for optical frequency domain imaging," Opt. Express **20**(22), 24132–24138 (2012).
8. T. Wang, W. Wieser, G. Springeling, R. Beurskens, C. T. Lancee, T. Pfeiffer, A. F. W. van der Steen, R. Huber, and G. van Soest, "Intravascular optical coherence tomography imaging at 3200 frames per second," Opt. Lett. **38**(10), 1715–1717 (2013).

#225855 - $15.00 USD Received 28 Oct 2014; revised 12 Jan 2015; accepted 13 Jan 2015; published 4 Feb 2015

9. T. Chen, N. Zhang, T. Huo, C. Wang, J. G. Zheng, T. Zhou, and P. Xue, "Tiny endoscopic optical coherence tomography probe driven by a miniaturized hollow ultrasonic motor," J. Biomed. Opt. **18**(8), 86011 (2013).
10. T.-H. Tsai, B. Potsaid, Y. K. Tao, V. Jayaraman, J. Jiang, P. J. S. Heim, M. F. Kraus, C. Zhou, J. Hornegger, H. Mashimo, A. E. Cable, and J. G. Fujimoto, "Ultrahigh speed endoscopic optical coherence tomography using micromotor imaging catheter and VCSEL technology," Biomed. Opt. Express **4**(7), 1119–1132 (2013).
11. H. S. Cho, S.-J. Jang, K. Kim, A. V. Dan-Chin-Yu, M. Shishkov, B. E. Bouma, and W.-Y. Oh, "High frame-rate intravascular optical frequency-domain imaging in vivo," Biomed. Opt. Express **5**(1), 223–232 (2013).
12. D. Lorenser, X. Yang, R. W. Kirk, B. C. Quirk, R. A. McLaughlin, and D. D. Sampson, "Ultrathin side-viewing needle probe for optical coherence tomography," Opt. Lett. **36**(19), 3894–3896 (2011).
13. S. Liang, A. Saidi, J. Jing, G. Liu, J. Li, J. Zhang, C. Sun, J. Narula, and Z. Chen, "Intravascular atherosclerotic imaging with combined fluorescence and optical coherence tomography probe based on a double-clad fiber combiner," J. Biomed. Opt. **17**(7), 070501 (2012).
14. J. Mavadia, J. Xi, Y. Chen, and X. Li, "An all-fiber-optic endoscopy platform for simultaneous OCT and fluorescence imaging," Biomed. Opt. Express **3**(11), 2851–2859 (2012).
15. D. Lorenser, B. C. Quirk, M. Auger, W.-J. Madore, R. W. Kirk, N. Godbout, D. D. Sampson, C. Boudoux, and R. A. McLaughlin, "Dual-modality needle probe for combined fluorescence imaging and three-dimensional optical coherence tomography," Opt. Lett. **38**(3), 266–268 (2013).
16. A. M. Fard, P. Vacas-Jacques, E. Hamidi, H. Wang, R. W. Carruth, J. A. Gardecki, and G. J. Tearney, "Optical coherence tomography - near infrared spectroscopy system and catheter for intravascular imaging," Opt. Express **21**(25), 30849–30858 (2013).
17. H. Pahlevaninezhad, A. M. D. Lee, T. Shaipanich, R. Raizada, L. Cahill, G. Hohert, V. X. D. Yang, S. Lam, C. MacAulay, and P. Lane, "A high-efficiency fiber-based imaging system for co-registered autofluorescence and optical coherence tomography," Biomed. Opt. Express **5**(9), 2978–2987 (2014).
18. M. R. Hee, E. A. Swanson, J. G. Fujimoto, and D. Huang, "Polarization-sensitive low-coherence reflectometer for birefringence characterization and ranging," J. Opt. Soc. Am. B **9**, 903–908 (1992).
19. J. F. de Boer, T. E. Milner, and J. S. Nelson, "Determination of the depth-resolved Stokes parameters of light backscattered from turbid media by use of polarization-sensitive optical coherence tomography," Opt. Lett. **24**(5), 300–302 (1999).
20. C. E. Saxer, J. F. de Boer, B. H. Park, Y. Zhao, Z. Chen, and J. S. Nelson, "High-speed fiber based polarization-sensitive optical coherence tomography of in vivo human skin," Opt. Lett. **25**(18), 1355–1357 (2000).
21. B. H. Park, C. Saxer, S. M. Srinivas, J. S. Nelson, and J. F. de Boer, "In vivo burn depth determination by high-speed fiber-based polarization sensitive optical coherence tomography," J. Biomed. Opt. **6**(4), 474–479 (2001).
22. Y. Yasuno, S. Makita, Y. Sutoh, M. Itoh, and T. Yatagai, "Birefringence imaging of human skin by polarization-sensitive spectral interferometric optical coherence tomography," Opt. Lett. **27**(20), 1803–1805 (2002).
23. M. Pircher, E. Götzinger, R. Leitgeb, H. Sattmann, O. Findl, and C. Hitzenberger, "Imaging of polarization properties of human retina in vivo with phase resolved transversal PS-OCT," Opt. Express **12**(24), 5940–5951 (2004).
24. J. Strasswimmer, M. C. Pierce, B. H. Park, V. Neel, and J. F. de Boer, "Polarization-sensitive optical coherence tomography of invasive basal cell carcinoma," J. Biomed. Opt. **9**(2), 292–298 (2004).
25. K. H. Kim, B. H. Park, Y. Tu, T. Hasan, B. Lee, J. Li, and J. F. de Boer, "Polarization-sensitive optical frequency domain imaging based on unpolarized light," Opt. Express **19**(2), 552–561 (2011).
26. L. P. Hariri, M. Villiger, M. B. Applegate, M. Mino-Kenudson, E. J. Mark, B. E. Bouma, and M. J. Suter, "Seeing beyond the Bronchoscope to Increase the Diagnostic Yield of Bronchoscopic Biopsy," Am. J. Respir. Crit. Care Med. **187**(2), 125–129 (2013).
27. X. Fu, Z. Wang, H. Wang, Y. T. Wang, M. W. Jenkins, and A. M. Rollins, "Fiber-optic catheter-based polarization-sensitive OCT for radio-frequency ablation monitoring," Opt. Lett. **39**(17), 5066–5069 (2014).
28. M. J. Suter, S. K. Nadkarni, G. Weisz, A. Tanaka, F. A. Jaffer, B. E. Bouma, and G. J. Tearney, "Intravascular optical imaging technology for investigating the coronary artery," JACC Cardiovasc. Imaging **4**(9), 1022–1039 (2011).
29. Y. Lim, Y.-J. Hong, L. Duan, M. Yamanari, and Y. Yasuno, "Passive component based multifunctional Jones matrix swept source optical coherence tomography for Doppler and polarization imaging," Opt. Lett. **37**(11), 1958–1960 (2012).
30. B. Baumann, W. Choi, B. Potsaid, D. Huang, J. S. Duker, and J. G. Fujimoto, "Swept source/Fourier domain polarization sensitive optical coherence tomography with a passive polarization delay unit," Opt. Express **20**(9), 10229–10241 (2012).
31. N. Daniel, S. Luke, L. Huiping, K. Tom, C. Fan, F. Steve, B. Glenn, and P. Simon, "Compact polarization diverse receiver for Biomed. imaging applications," in *Design and Quality for Biomedical Technologies IV*, R. Ramesh, and L. Rongguang, eds. (2011), p. 78910Q.
32. S. J. Frisken and D. R. Neill, "Optical coherence tomography system and method," (US patent 20120120407).
33. A. M. D. Lee, H. Pahlevaninezhad, V. X. D. Yang, S. Lam, C. MacAulay, and P. Lane, "Fiber-optic polarization diversity detection for rotary probe optical coherence tomography," Opt. Lett. **39**(12), 3638–3641 (2014).
34. E. Z. Zhang and B. J. Vakoc, "Polarimetry noise in fiber-based optical coherence tomography instrumentation," Opt. Express **19**(18), 16830–16842 (2011).

#225855 - $15.00 USD Received 28 Oct 2014; revised 12 Jan 2015; accepted 13 Jan 2015; published 4 Feb 2015

35. E. Z. Zhang, W.-Y. Oh, M. L. Villiger, L. Chen, B. E. Bouma, and B. J. Vakoc, "Numerical compensation of system polarization mode dispersion in polarization-sensitive optical coherence tomography," Opt. Express **21**(1), 1163–1180 (2013).
36. M. Villiger, E. Z. Zhang, S. Nadkarni, W.-Y. Oh, B. E. Bouma, and B. J. Vakoc, "Artifacts in polarization-sensitive optical coherence tomography caused by polarization mode dispersion," Opt. Lett. **38**(6), 923–925 (2013).
37. C. R. Menyuk and A. Galtarossa, *Polarization Mode Dispersion* (Springer, 2005).
38. M. Villiger, E. Z. Zhang, S. K. Nadkarni, W.-Y. Oh, B. J. Vakoc, and B. E. Bouma, "Spectral binning for mitigation of polarization mode dispersion artifacts in catheter-based optical frequency domain imaging," Opt. Express **21**(14), 16353–16369 (2013).
39. J. Roth, "Poincare sphere plot of polarimetry Stokes vectors," (MATLAB Central File Exchange, http://www.mathworks.nl/matlabcentral/fileexchange/10979-poincare-sphere-plot-of-polarimetry-stokes-vectors/content/poincare.m).
40. E. Götzinger, M. Pircher, B. Baumann, T. Schmoll, H. Sattmann, R. A. Leitgeb, and C. K. Hitzenberger, "Speckle noise reduction in high speed polarization sensitive spectral domain optical coherence tomography," Opt. Express **19**(15), 14568–14585 (2011).
41. Y. Lim, M. Yamanari, S. Fukuda, Y. Kaji, T. Kiuchi, M. Miura, T. Oshika, and Y. Yasuno, "Birefringence measurement of cornea and anterior segment by office-based polarization-sensitive optical coherence tomography," Biomed. Opt. Express **2**(8), 2392–2402 (2011).
42. Z. Lu, D. K. Kasaragod, and S. J. Matcher, "Method to calibrate phase fluctuation in polarization-sensitive swept-source optical coherence tomography," J.Biomed.Opt. **16**, 070502–070502–070503 (2011).
43. B. Braaf, K. A. Vermeer, M. de Groot, K. V. Vienola, and J. F. de Boer, "Fiber-based polarization-sensitive OCT of the human retina with correction of system polarization distortions," Biomed. Opt. Express **5**(8), 2736–2758 (2014).
44. Z. Wang, H.-C. Lee, O. O. Ahsen, B. Lee, W. Choi, B. Potsaid, J. Liu, V. Jayaraman, A. Cable, M. F. Kraus, K. Liang, J. Hornegger, and J. G. Fujimoto, "Depth-encoded all-fiber swept source polarization sensitive OCT," Biomed. Opt. Express **5**(9), 2931–2949 (2014).
45. M. J. Ju, Y.-J. Hong, S. Makita, Y. Lim, K. Kurokawa, L. Duan, M. Miura, S. Tang, and Y. Yasuno, "Advanced multi-contrast Jones matrix optical coherence tomography for Doppler and polarization sensitive imaging," Opt. Express **21**(16), 19412–19436 (2013).
46. J. Li and J. F. de Boer, "Coherent signal composition and global phase determination in signal multiplexed polarization sensitive optical coherence tomography," Opt. Express **22**(18), 21382–21392 (2014).
47. B. H. Park, M. C. Pierce, B. Cense, and J. F. de Boer, "Jones matrix analysis for a polarization-sensitive optical coherence tomography system using fiber-optic components," Opt. Lett. **29**(21), 2512–2514 (2004).
48. M. Pierce, M. Shishkov, B. Park, N. Nassif, B. Bouma, G. Tearney, and J. de Boer, "Effects of sample arm motion in endoscopic polarization-sensitive optical coherence tomography," Opt. Express **13**(15), 5739–5749 (2005).
49. M. Born and E. Wolf, *Principles of Optics* (Cambridge University, 1999).

1. Introduction

Optical coherence tomography (OCT) is an optical imaging technique which can acquire non-invasive high resolution cross sectional images in real time [1]. OCT imaging has been proven particularly effective for clinical diagnosis in ophthalmology [2]. The combination of OCT and endoscopy, namely endoscopic OCT, is a significant leap that broadens the application of OCT to hollow organs [3–5]. The recent development of endoscopic OCT towards smaller, faster and functional [6–12] and multimodal systems [13–17], further provides clinicians with improved contrast for more comprehensive and accurate diagnosis.

Polarization sensitive OCT (PS-OCT) is an extension of conventional OCT that in addition to tissue structure can image tissue birefringence to provide extra tissue specifying information, making it a promising functional extension of conventional OCT [18–26]. Catheter based PS-OCT [27] is a relatively new area which encounters several challenges. One notable issue is how to mitigate the polarization state changes when light travels through an optical fiber in the rapidly scanning catheter [28].

In this paper we demonstrate a polarization sensitive endoscopic optical frequency domain imaging (OFDI) system with a distal scanning miniature catheter. Structural and Jones matrix based phase retardation images are acquired of ex vivo chicken sample, in vivo pig lung and ex vivo human lung specimens. Technical issues such as complex field averaging and polarization state stability are also discussed in depth.

#225855 - $15.00 USD Received 28 Oct 2014; revised 12 Jan 2015; accepted 13 Jan 2015; published 4 Feb 2015

2. Method

2.1 Experiment setup overview

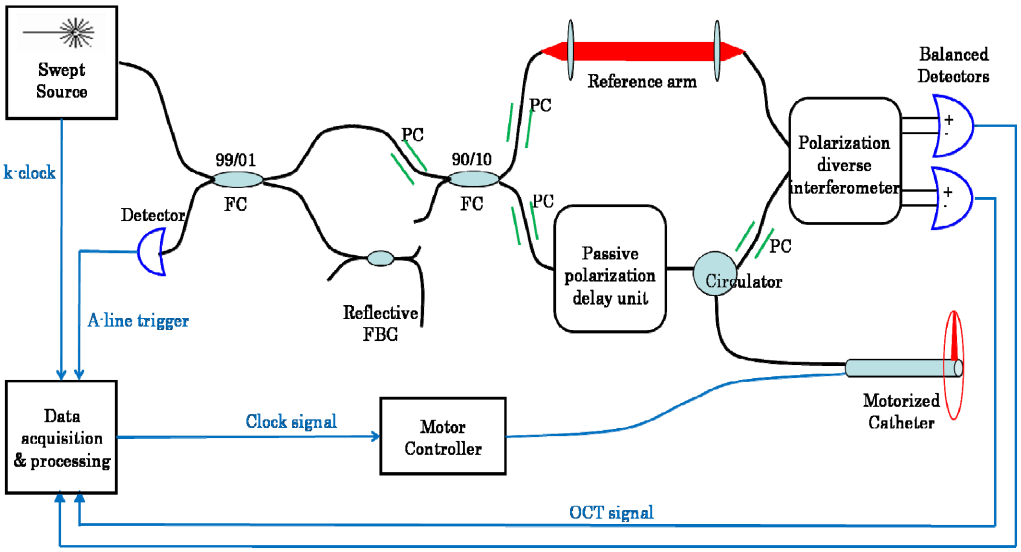

Fig. 1. Endoscopic PS-OFDI System schematic. FC: fiber-optic coupler, PC: polarization controller, FBG: fiber Bragg grating.

The schematic of the endoscopic PS-OFDI system is shown in Fig. 1. It is modified from the system demonstrated in our previous work [7]. A 99/01 coupler is added between the swept source (Axsun Technologies Inc., 1310nm 50kHz) and the interferometer to split a tiny portion of light to the fiber Bragg grating (FBG, O/E land Inc.). The FBG reflects at 1266nm, providing a phase stable A-line trigger to the data acquisition card (Alazar Technologies Inc., ATS9350). A passive polarization delay unit (PDU) similar to those reported by [29, 30] is added to the sample arm to multiplex two orthogonal incident polarization states in depth. With such multiplexing the effective imaging range is 2.5 mm, coming from the fact that the 5 mm ranging depth is multiplexed over two polarization states. We employed single mode fiber (SM28) throughout the system. The fiber length in the reference arm and the sample arm are matched within 1 centimeter range to minimize chromatic dispersion. The length of optical fiber and the electrical cable of the k-clock signal were carefully matched to eliminate the dispersion caused by the combination of a different propagation delay to the data acquisition board of these signals and the non-linear wavelength sweep.

The bulk-optic polarization diverse detection unit is replaced by a compact polarization-diversity receiver module (NinePoint Medical, Cambridge, Massachusetts). The unit splits the reference and sample arm light into orthogonal components before interfering the sample and reference arm light The orthogonal interference channels are coupled into graded index multi-mode fibers (GI-50) to minimize the insertion loss [31, 32]. The wavelength-dependent splitting ratio of the micro-optic assembly is low, allowing for balanced-detection at relative high reference arm powers (Fig. 2). A similar unit has been reported by Lee et. al [33] for fixing the variation of OCT image intensity due to the change of polarization states during imaging.

We quantified the flatness of the balanced spectra by a dimensionless ratio r. For each detector,

$$r = \frac{\langle I_{\text{var}} \rangle}{\langle I_{total} \rangle}, \quad \langle I_{\text{var}} \rangle = \sqrt{\left\langle \left(I(\lambda) - \langle I(\lambda) \rangle \right)^2 \right\rangle}.$$

#225855 - $15.00 USD Received 28 Oct 2014; revised 12 Jan 2015; accepted 13 Jan 2015; published 4 Feb 2015

where angled brackets denote averaging over wavelength, $I(\lambda)$ is the wavelength dependent optical power difference after the balanced receiver, and $\langle I_{total} \rangle$ is the sum of the averaged power received by the two input leads of the balanced receiver during the wavelength sweep of the 50% duty cycle. Since the power of the back scattered light in the sample arm is far lower than the power of the light in the reference arm, $\langle I_{total} \rangle$ is completely dominated by the reference arm power (1.7 mW). For the horizontal (H) and vertical (V) detectors the ratio r was $r_H = 0.005$ and $r_V = 0.004$, respectively.

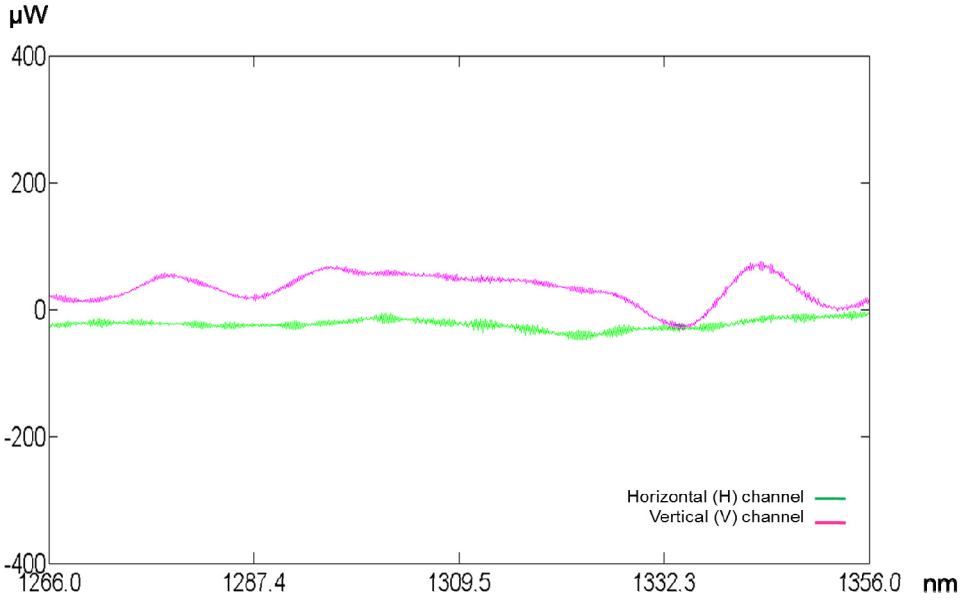

Fig. 2. Balanced spectra of reference arm input. Horizontal axis: wavelength. Vertical axis: Balanced power at the receiver. Green trace: spectrum acquired by the horizontal (H) channel; Magenta trace: spectrum acquired by the vertical (V) channel.

It has been demonstrated that polarization mode dispersion (PMD), i.e. the difference in the propagation characteristics of light waves with different polarization states, can cause blurring of the OCT structural image and can lead to significant artifacts in birefringence images [34–36]. Moreover, the so-called second order PMD has wavelength dependence [37]. The optical circulator is a known cause of PMD [35]. Thus we converted the reference arm from reflection-type to transmission-type to eliminate one circulator. We evaluated the PMD in the system by monitoring the evolution of the Stokes vector as a function of wavelength [35] for a simple reflector. The angle $\Delta\phi$ spanned by the trace of the Stokes vector in the Poincare sphere is jointly determined by the differential group delay (DGD) $\Delta\tau$ and bandwidth of the source $\Delta\omega$,

$$\Delta\phi = \Delta\tau \cdot \Delta\omega.$$

$\Delta\omega$ is related to wavelength sweep range $\Delta\lambda$ through

$$\Delta\omega = 2\pi c\Delta\lambda / \lambda_0^2 .$$

Accordingly, the DGD

$$\Delta\tau = \Delta\phi / \Delta\omega = \Delta\phi\lambda_0^2 / 2\pi c\Delta\lambda .$$

#225855 - $15.00 USD Received 28 Oct 2014; revised 12 Jan 2015; accepted 13 Jan 2015; published 4 Feb 2015

With a Thorlabs CIR1310 fiber optical circulator in the sample arm we measured approximately $\Delta\phi = \frac{\pi}{2}$ (Fig. 3), resulting in a DGD of $\Delta\tau = 0.018\,\text{ps}$ (roundtrip). This quantity corresponds to a broadening of the interference peak $\Delta z = \frac{c \cdot \Delta\tau}{2n} = 2.0\,\mu\text{m}$, with n the refractive index of water and the factor 2 accounting for the roundtrip. This is smaller than the nominal depth resolution of the system, which was measured to be 15.6 μm (Full Width at Half Maximum) in air, giving 11.7 μm in tissue (n = 1.33). Zhang and Villiger introduced a 0.087 ps DGD to study the effect of DGD on polarization sensitive imaging [35, 36], and concluded that a PMD smaller than the axial resolution was not a serious issue. Therefore PMD correction [35] or mitigation [38] was not included.

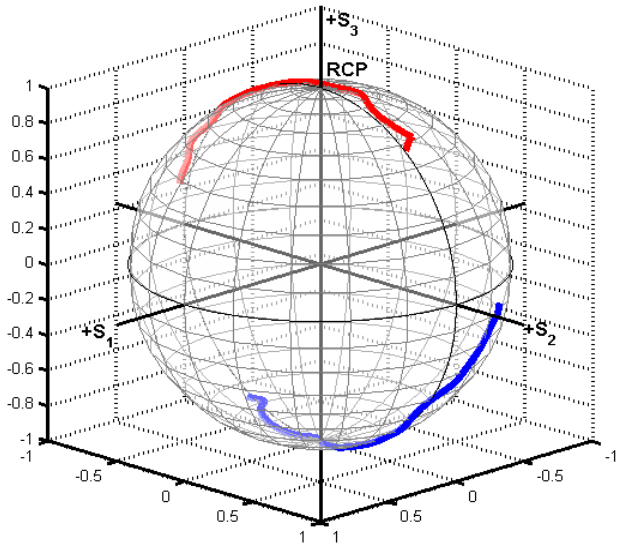

Fig. 3. Stokes vector representation of the evolution of a reflected state from the sample arm as a function of wavelength, rendered through open access MatLab code [39]. Blue trace: state 1; Red trace: state 2.

The procedure for calibrating the polarization controllers prior to imaging was as follows: 1. Control the polarization controller in the reference arm to equalize the power received by detector H and V; 2. Connect the catheter into the sample arm, control the polarization controller before the PDU to equalize the power going into the two orthogonal incident states. Here the peak height of the reflection on the catheter surface is a good reference. In total four electric fields, the two multiplexed states mapped on the two detection channels ($H_{1,2}$ and $V_{1,2}$), are recorded for each sampling point.

The motorized distal scanning miniature catheter is identical to the one described in [7] where different versions are available for animal and human use. A home-made motor driver drives the scanning at 3120 rpm, i.e. the B-scan rate is 52 fps.

2.2 Complex field averaging

In order to reduce speckle noise and improve the output of the polarization sensitive measurement, we explored a complex electric field averaging technique. Several averaging methods have been suggested previously, either on Jones matrices or Stokes vector, or other parameters that relate to birefringence [40–44]. A difficulty lying at the core of field averaging techniques is the so called global phase [41, 45, 46], which comprises the

#225855 - $15.00 USD Received 28 Oct 2014; revised 12 Jan 2015; accepted 13 Jan 2015; published 4 Feb 2015

randomness of multiple sources of phase instability. Such sources include phase fluctuation in the reference and sample arms and the fact that photon scattering happens at arbitrary locations within the axial resolution, giving the reflected field an arbitrary phase. Recently we derived the exact form of the global phase for the determinant of the complex Jones matrix; however, the global phase determined from the determinant of the complex Jones matrix suffers from a π angle ambiguity which needs further treatment [46].

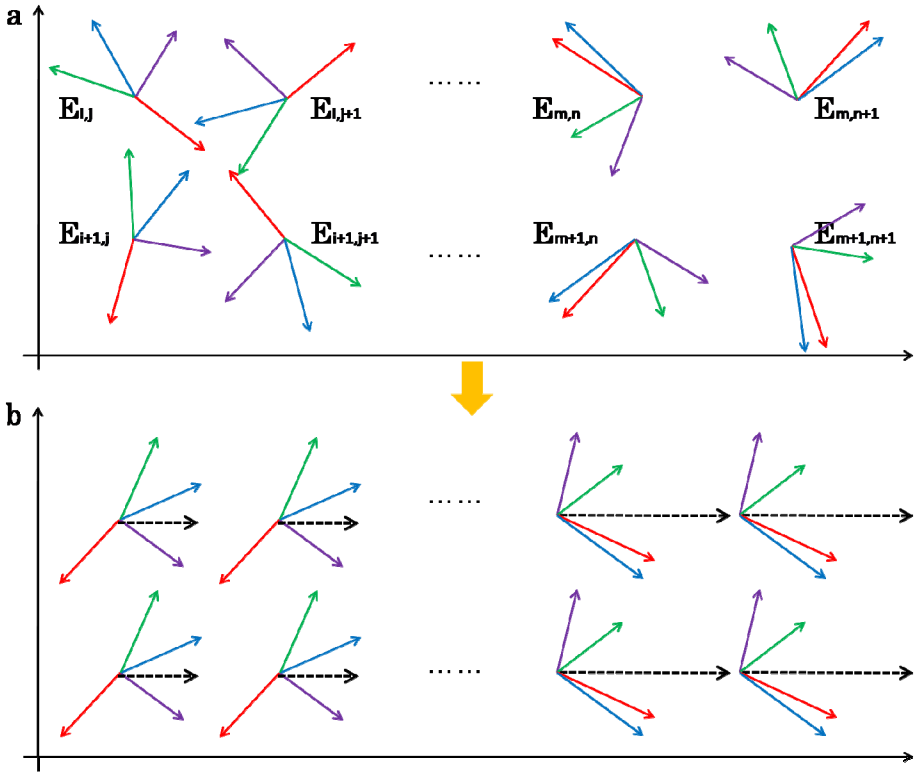

Fig. 4. Diagram of field phasor alignment. For each sampling point there is a field matrix E consisting of four field phasors. (a) The neighboring points have similar relative phase angles between these phasors, though global phase adds random rotation on all of them. (b) By aligning the vector sum of the four phasors to the positive real axis, the neighboring phasors are aligned correspondingly. The colored arrows represent field phasors. The dash arrow represents the vector sum of the four phasors.

Therefore we developed an averaging approach where the field components are treated as phasors. The sum of the four complex field components of each pixel is aligned to the positive real axis prior to averaging. The angle Θ of the phasor sum $H_1 + H_2 + V_1 + V_2$ is determined as,

$$\Theta = \arctan\left(\frac{\mathrm{Im}\left(H_1 + H_2 + V_1 + V_2\right)}{\mathrm{Re}\left(H_1 + H_2 + V_1 + V_2\right)}\right).$$

and the complex field components $H_{1,2}$ and $V_{1,2}$ are aligned by multiplying with $e^{-i\cdot\Theta}$. Figure 4 illustrates the concept of this method. Birefringence changes the relative angle between the field components, and therefore a key precondition is that the birefringence only slowly changes the relative phase angles among these complex field components over the averaging area, which is generally valid. After the alignment the same field components of the Jones

#225855 - $15.00 USD Received 28 Oct 2014; revised 12 Jan 2015; accepted 13 Jan 2015; published 4 Feb 2015

matrix of neighboring pixels share similar phase angles. A field averaging relatively local in both the axial and lateral direction can be performed to improve the SNR of the measured fields.

The ability to average field components provides more flexibility later on, e.g. to have a higher degree of averaging for the surface of the tissue to achieve a more reliable reference surface state for the tissue birefringence calculation.

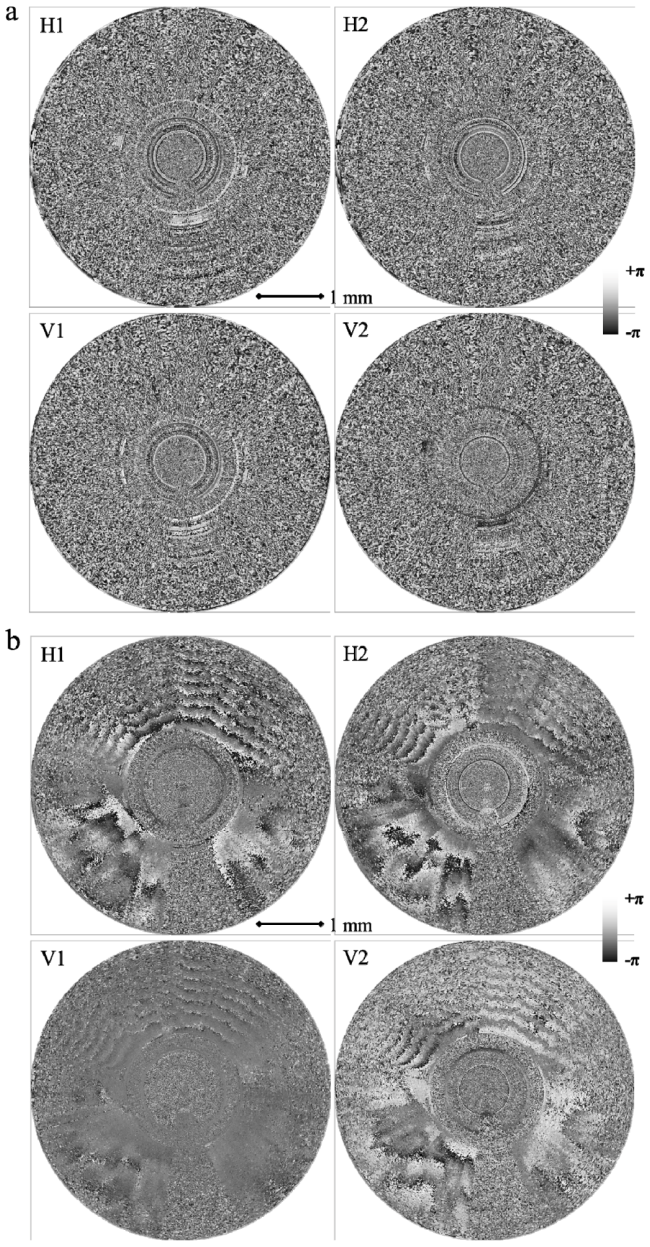

Fig. 5. Absolute phases of $H_1 + H_2 + V_1 + V_2$ components of a B-scan measurement, before (a) and after (b) phasor alignment. The grayscale ranges from -π to + π. It is clearly seen that before the alignment the phases are totally random while after the alignment the phases have only slow variation due to tissue birefringence.

#225855 - $15.00 USD Received 28 Oct 2014; revised 12 Jan 2015; accepted 13 Jan 2015; published 4 Feb 2015

To demonstrate the effect of global phase correction the phasor method was applied to a measurement of fresh chicken. Figure 5 shows images of the phase angle of the four electric phasors before and after applying the global phase correction. It is clearly seen that after the alignment the global randomness of the phases is eliminated, leaving only the effect of tissue birefringence.

The phasor sum alignment approach is similar to the ones proposed by Yasuno [41] and Braaf [43], except that we do not define a moving kernel and not choose a reference pixel with highest SNR. The alignment is applied once to all pixels.

2.3 Image processing algorithm

The data from horizontal (H) and vertical (V) detectors are processed frame by frame. The mean trace of 960 A-lines composing a single frame is firstly subtracted from each trace to remove DC background and fixed pattern noise and a cosine tapered window is applied. To compensate chromatic dispersion, the required phase function was determined from the reflection signal on the surface of the catheter sheath beforehand and applied here. The 1024 points trace is then lengthened to 4096 points by zero padding and Fourier transformed into an A-line. The positive frequency part of the A-line is divided in the middle to separate the two incident polarization states. Since this does not guarantee pixel-to-pixel alignment of the two states, a cross correlation is applied to calculate the mismatch and a circular shift is applied to the second field to correct the mismatch. The surfaces of the catheter are searched based on their geometrical feature. Then the random phase correction and field averaging as described above were implemented.

To determine the round trip retardation of the tissue, we use the Jones formalism that has been widely used [47, 29, 30, 44, 45]. The incident field matrix $E_{in} = \begin{bmatrix} H_{in}^1 & H_{in}^2 \\ V_{in}^1 & V_{in}^2 \end{bmatrix}$ evolves to $E_{out} = \begin{bmatrix} H_{out}^1 & H_{out}^2 \\ V_{out}^1 & V_{out}^2 \end{bmatrix}$ as described by the total Jones matrix $J(z) = J_{out} J_s(z) J_{in}$. Thus, $E_{out}(z) = J(z) E_{in}$. Here $J_s(z)$ is the roundtrip sample Jones matrix for signal scattered at the depth of z. J_{in} and J_{out} are inbound and outbound system Jones matrices. It is obvious that at the surface of the sample $E_{out}(z) = J_{out} J_{in} E_{in}$. Therefore $E_{out}(z) \cdot E_{out}^{-1}(z_0) = J_{out} J_s(z) J_{in} E_{in} E_{in}^{-1} J_{in}^{-1} J_{out}^{-1} = J_{out} J_s(z) J_{out}^{-1}$. Since J_{out} and J_{out}^{-1} are unitary matrices, $J_{out} J_s(z) J_{out}^{-1}$ has same eigenvalues as $J_s(z)$, denoted as λ_1 and λ_2 . Sample birefringence can be determined from the eigenvalues as $\arctan(\frac{im(\lambda_1 \lambda_2)}{re(\lambda_1 \lambda_2)})$.

The surface of the catheter is chosen as the reference surface to determine electric fields at the surface of the sample. 6x6 points field averaging is applied for the whole image, while 10x6 points averaging (lateral x axial) is applied for the reference surface. The structural OCT image is processed with the determinant method described earlier in [46] for better SNR, plus a 4x4 median filter to reduce speckle noise.

2.4 Change in incident polarization state

With the polarization sensitive detection unit and the above stated sample surface referencing method, we expect that the change in incident polarization state during imaging is not an issue for both the intensity image and the birefringence image. Nevertheless, we quantified the changes of the surface polarization state to compare it with the proximal scanning catheter [48]. For both the inner and outer surfaces of the catheter sheath, the Stokes parameters Q, U and V of the two incident states are recorded for a full B-scan. The results are shown in Fig. 6.

#225855 - $15.00 USD Received 28 Oct 2014; revised 12 Jan 2015; accepted 13 Jan 2015; published 4 Feb 2015

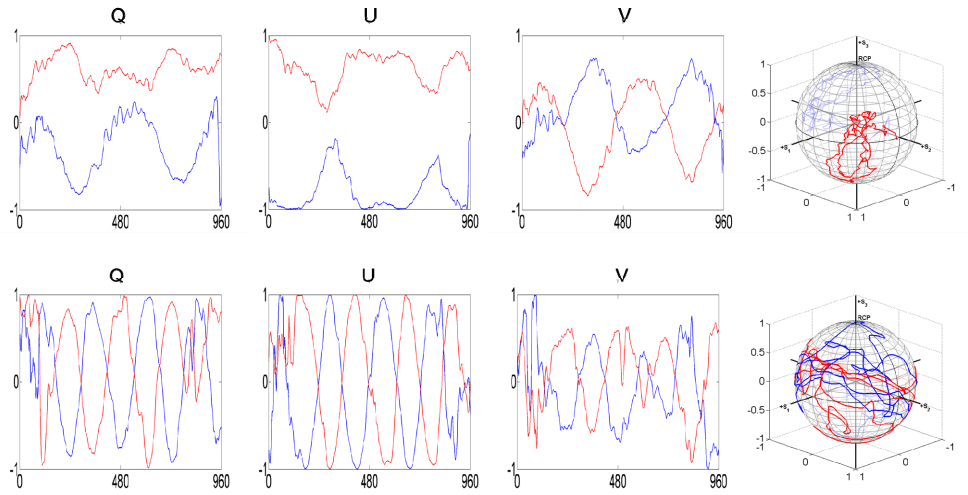

Fig. 6. Measured Stokes parameters and trace of Stokes vectors for a whole B-scan (960 A-lines) for Fresnel reflection signals on the inner (top row) and outer (bottom row) surface of the sheath. Blue trace: state 1; Red trace: state 2.

The surface polarization states for the inner and outer surface of the catheter sheath differed significantly. First of all, the fiber in the sample arm is static during scanning (Fig. 7). Therefore the polarization state changes with respect to the inner surface reflection must be attributed to birefringence changes that are caused by the change of the orientation of the reflective mirror mounted on the motor. The phase shift between two polarization states reflected from a metallic surface is a well-known effect [49]. The amount of phase shift depends on the complex refractive index of the surface substrate of the mirror, the incident angle of the beam, and the relative angle of the polarization plane with reference to the mirror. Maximum difference of the phase shifts occurs when the beam is incident at 45 degree, which approximates the situation in our catheter. However, the azimuthal scanning of the mirror constantly alters the relative angle of the two polarization planes for the beam coming out of the GRIN. Consequently a variation emerges for the polarization states measured at the inner surface of the catheter sheath. For the outer surface of the sheath, a certain amount of birefringence of the Pebax material must be added into the model, together with the above stated phase shift resulting in a variation that draws a bigger loop on the Poincare sphere.

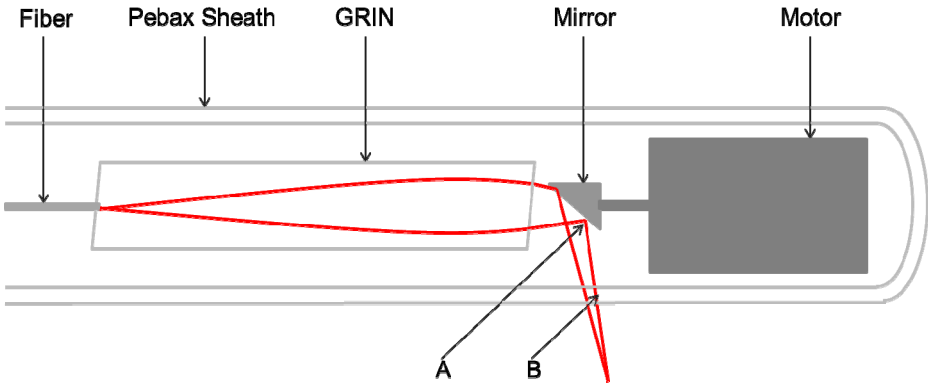

Fig. 7. Schematic diagram of the optics of the catheter. For simplicity, accessorial holders and motor wires are not shown. Polarization state changes occur predominantly at A: reflection on metallic mirror; and B: propagation in Pebax sheath.

#225855 - $15.00 USD Received 28 Oct 2014; revised 12 Jan 2015; accepted 13 Jan 2015; published 4 Feb 2015

For endoscopic imaging the outer surface of the sheath usually is in contact with the tissue, causing refractive index matching condition. Therefore the Fresnel reflection from the outer surface is usually weaker than that from the inner surface. This could be a practical reason for using the inner surface as the reference surface for determining tissue birefringence [44]. However, as we can see above, the catheter sheath itself can have considerable birefringence. Accordingly using the inner surface risks from introducing artifacts to the tissue retardation measurement. The use of the outer surface will not suffer from the catheter sheath birefringence. Moreover, we measured empirically 40 dB and 36 dB SNR at the inner and outer surfaces in one of our experiment where the catheter closely contacted with human bronchus tissue, which suggests the SNR difference is not crucial. Hence we always choose the outer surface as the reference surface, combined with field averaging to improve the SNR of the surface polarization states.

3. Results

Before carrying out animal test, we first verified the system by imaging a fresh chicken sample. The sample was covered by cling film and wrapped around the catheter. It contains both muscles and tendons. Figure 8 shows the intensity image and phase retardation images with and without prior complex field averaging. It can be observed that the averaging does reduce the speckle noise and improve the visibility of the image. The averaging procedure was implemented in all subsequent images.

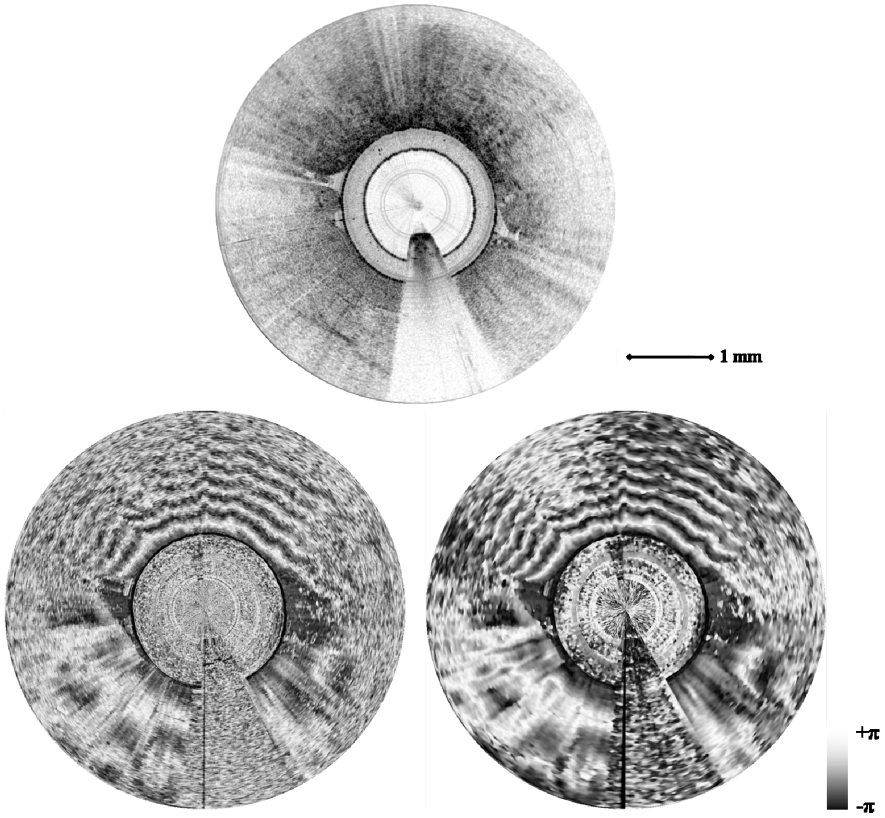

Fig. 8. Images of ex vivo chicken muscle and tendon. Top: structural image; Bottom-left: phase retardation image without field averaging; Bottom-right: phase retardation image with field averaging. For the phase retardation images the grayscale ranges from -π to + π. Position between 5 o'clock and 6 o'clock is blocked by the motor wires.

#225855 - $15.00 USD Received 28 Oct 2014; revised 12 Jan 2015; accepted 13 Jan 2015; published 4 Feb 2015

An in vivo imaging test with live pig was then conducted (Fig. 9). The entire system was built in a mobile cart and transported to the animal operation room. The pig was anesthetized and imaged by bronchoscopy. The OFDI catheter was inserted through the biopsy channel of the bronchoscope and images were acquired with manual pull-back at a speed of approximately 1 mm/s. Layered structure, which mainly consists of the layers of epithelium, lamina propria, cartilage and sub mucosa, can be visualized on the structural OFDI image. Meanwhile the phase retardation image indicates regions with strong birefringence.

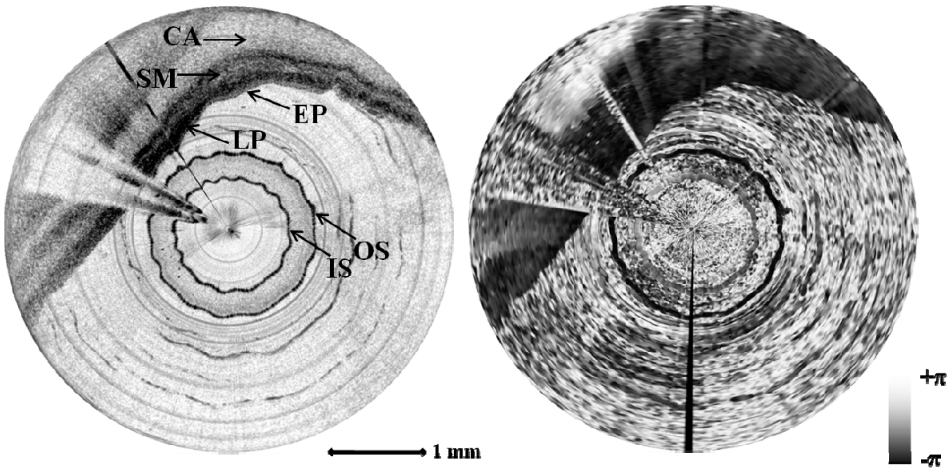

Fig. 9. Image of in vivo pig bronchus. Left: structural image; Right: phase retardation image. Position between 9 o'clock and 10 o'clock is blocked by the motor wires. EP: epithelium, LP: lamina propria, SM: submucosa, CA: cartilage. IS/OS: Inner/Outer surface of catheter sheath. Videos are available online (Media 1 and Media 2).

The images acquired in ex vivo human bronchi specimen provide similar information (Fig. 10). For this test, the system was transported the autopsy room in the university hospital. The catheter reserved for human research was used. Lung specimens were obtained from a 67-year old female with no recorded lung diseases. Several specimens were imaged on site. The manual pull-back speed was also about 1 mm/s. To further understand the structural image and pinpoint the tissue that exhibit strong birefringence, histology is necessary, which was not available for the imaged section.

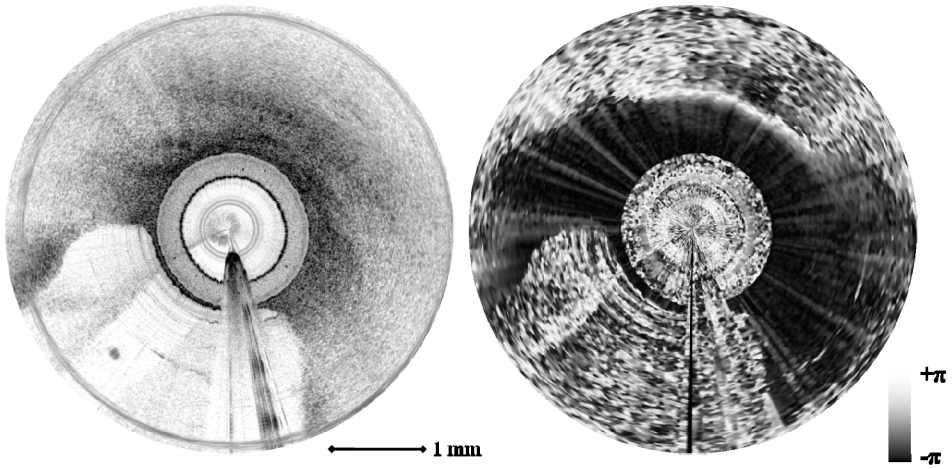

Fig. 10. Image of ex vivo human bronchus. Left: structural image; Right: phase retardation image. Position between 5 o'clock and 6 o'clock is blocked by the motor wires.

#225855 - $15.00 USD Received 28 Oct 2014; revised 12 Jan 2015; accepted 13 Jan 2015; published 4 Feb 2015

4. Conclusion

In this study a polarization sensitive optical frequency domain imaging system with distal scanning endoscopic catheter is demonstrated. Technical aspects including balanced detection, polarization mode dispersion, and variation of incident polarization states are characterized. In order to reduce speckle noise and improve quality of phase retardation measurement, a complex field averaging approach was adopted. This approach is relatively simple and takes effect globally for the whole data set. Biological samples such as ex vivo chicken, in vivo pig bronchus and ex vivo human lung specimens are scanned for both structural and phase retardation images. The phase retardation images show correspondence, indicating strong birefringence exists in certain layers in bronchus tissue. To understand such correspondence in depth, further investigation with histology correlation is needed. Nevertheless, we believe the polarization sensitive endoscopic optical frequency domain imaging will open up a new route in image based diagnosis of lung disease.

Acknowledgments

We gratefully acknowledge financial support from LaserLaB Amsterdam, Laserlab-Europe (EC-GA 284464), the Netherlands Organization for Scientific Research (NWO) with a Vici (JFdB) and an NWO-Groot grant (JFdB). This work is part of the research program of the Foundation for Fundamental Research on Matter (FOM), which is part of the Netherlands Organization for Scientific Research (NWO). F. Feroldi thanks the Netherlands Organization for Health Research and Development (ZonMw) for funding his position. The authors thank B. Braaf, D. van Iperen and J.J. Weda for useful discussions.

#225855 - $15.00 USD Received 28 Oct 2014; revised 12 Jan 2015; accepted 13 Jan 2015; published 4 Feb 2015